SOLAR DYNAMICS AND MAGNETISM

Active Region Formation through the Negative Effective Magnetic Pressure Instability

Koen Kemel · Axel Brandenburg · Nathan Kleeorin ·
Dhrubaditya Mitra · Igor Rogachevskii

Abstract The negative effective magnetic-pressure instability operates on scales encompassing many turbulent eddies, which correspond to convection cells in the Sun. This instability is discussed here in connection with the formation of active regions near the surface layers of the Sun. This instability is related to the negative contribution of turbulence to the mean magnetic pressure that causes the formation of large-scale magnetic structures. For an isothermal layer, direct numerical simulations and mean-field simulations of this phenomenon are shown to agree in many details, for example the onset of the instability occurs at the same depth. This depth increases with increasing field strength, such that the growth rate of this instability is independent of the field strength, provided the magnetic structures are fully contained within the domain. A linear stability analysis is shown to support this finding. The instability also leads to a redistribution of turbulent intensity and gas pressure that could provide direct observational signatures.

Keywords Magnetohydrodynamics (MHD) · Sun: dynamo · Sunspots · Turbulence

1. Introduction

Active-region formation in the Sun is traditionally thought to be a deeply rooted phenomenon, because their size ($\approx 100\,\mathrm{Mm}$) is much larger than the naturally occurring scales

K. Kemel (✉) · A. Brandenburg · N. Kleeorin · D. Mitra · I. Rogachevskii
Nordita, Royal Institute of Technology and Stockholm University, Roslagstullsbacken 23,
10691 Stockholm, Sweden
e-mail: brandenb@nordita.org

K. Kemel · A. Brandenburg
Department of Astronomy, Stockholm University, 10691 Stockholm, Sweden

N. Kleeorin · I. Rogachevskii
Department of Mechanical Engineering, Ben-Gurion University of the Negev, POB 653, Beer-Sheva
84105, Israel

in the surface layers of the convection zone ($\approx 1 - 10\,\mathrm{Mm}$); see Golub *et al.* (1981). They are also long-lived (several months), which seems unnaturally long if associated with the near-surface layers (40 Mm depth), where typical time scales are about a day. This is particularly true of what are called *complexes of activity*, which can live for $\approx 1/2$ year (Golub and Vaiana, 1980). At the bottom of the convection zone, or even beneath it in the tachocline, the typical timescales are long ($\approx$ one month) and it might then, at these depths, be easier to envisage mechanisms for producing recurrent eruptions including sunspots over timescales exceeding 1/2 year. A detailed report of recurrent sunspot activity between 23 August 1903 and 14 August 1904 was published by Epstein (1904), who referred to that region as a *Fleckenherd*, which can be translated as sunspot hearth. Later, Sanford (1941) referred to this as an *active region* and gave details about an event lasting 620 days from 20 August 1929 to 2 May 1931. In Epstein's early article, which was written in German,[1] he wrote that *a Fleckenherd is a region on the solar surface where sunspots (both larger and smaller ones, of shorter and longer duration) have occurred in a confined area for at least eight rotation periods.* Such regions on the Sun would nowadays be referred to as complexes of activity, while those discussed by Sanford (1941) would perhaps be called superactive regions or active zones (Bai, 1987, 1988), and might also be related to active longitudes (Vitinskij, 1969; Bogart, 1982).

All of these phenomena, from active regions to active longitudes, are probably caused by magnetic-flux enhancements of some sort. For the purpose of this article, we simply refer to them as active regions. Instabilities in the tachocline are generally held responsible for their formation such as the clamshell and tipping instabilities (Cally, Dikpati, and Gilman, 2003), which are global instabilities of a magnetic belt around the Sun. Based on calculations using the thin-fluxtube approximation, the field strength of such a magnetic belt is expected to be around $10^5\,\mathrm{G}$ (Choudhuri and Gilman, 1987; D'Silva and Choudhuri, 1993; Schüssler *et al.*, 1994); see Fan (2009) and Charbonneau (2010) for recent reviews on the subject. However, such strong fields may be unstable (Tayler, 1973); see Arlt, Sule, and Rüdiger (2007), who found $100\,\mathrm{G}$ to be the limit. A completely different idea is to invoke a coupling to non-axisymmetric dynamo modes (Ruzmaikin, 1998; Bigazzi and Ruzmaikin, 2004), but the field is still thought to reside near the bottom of the convection zone.

A general problem with deeply rooted active regions as a source of sunspots is the difficulty of keeping a buoyant flux tube intact, so that it can pierce through the surface to form a well-confined bipolar region. Another difficulty concerns the angular velocity of active regions. At the beginning of the solar cycle, at 30° latitude, they have a rotation rate of $\approx 446\,\mathrm{nHz}$, matching the local angular velocity at a radius of $\approx 0.95 R_\odot$, but exceeding the value at the bottom of the convection zone by $\approx 10\,\mathrm{nHz}$. Likewise, at the end of the cycle, at 4° latitude, they have a rotation rate of $\approx 462\,\mathrm{nHz}$, matching the local angular velocity near the surface at a radius of $\approx 0.97 R_\odot$, again exceeding the value at the bottom of the convection zone by $\approx 10\,\mathrm{nHz}$; see Figure 4 of Benevolenskaya *et al.* (1999) and Figure 2 of Brandenburg (2005). Other difficulties concern the high field strength in the tachocline required by thin-fluxtube calculations to explain the observed tilt angles (D'Silva and Choudhuri, 1993). On the other hand, Kosovichev and Stenflo (2008) pointed out that there is no

---

[1]We gave here a rather free translation of his original and somewhat antique formulation. For historical reasons, and for the benefit of those with restricted access to the original issue of *Astronomische Nachrichten*, we reproduce here his original definition: *Ein Fleckenherd auf der Sonne. So kann man füglich eine Gegend auf der Sonnenoberfläche bezeichnen, wo in einem verhältnismäßig beschränkten Bezirke im Verlaufe eine Jahres in mindestens acht Rotationen Flecke, teils größere, teils kleinere, teils von kürzerem, teils von längerem Bestande, aufgetreten sind. ...* [*Th. Epstein, Frankfurt am Main, Oktober 1904*]

evidence for a dependence of the tilt angle on magnetic-field strength, as expected based on thin-fluxtube calculations. Furthermore, Stenflo and Kosovichev (2012) find no indication of a dependence of the tilt angle on the size of the region, which one may expect if the tilts were produced by the Coriolis force during the buoyant rise of flux loops from the tachocline. Several of the arguments discussed above have led to the consideration of solar activity as a shallow phenomenon; see Brandenburg (2005) for details. Even sunspots themselves suggest their being rather shallow (Zhao, Kosovichev, and Duvall, 2001; Kosovichev, 2002). This raises the question whether there is then a mechanism that could be responsible for accumulating magnetic flux near the surface.

The idea of magnetic-field clustering has been discussed in the contexts of both deeply rooted (Ruzmaikin, 1998) and shallow (Schatten, 2007) dynamo scenarios that are now becoming more fashionable (Pipin and Kosovichev, 2011). Here we discuss the negative effective magnetic-pressure instability (Kleeorin, Rogachevskii, and Ruzmaikin, 1989, 1990; Kleeorin and Rogachevskii, 1994; Kleeorin, Mond, and Rogachevskii, 1996; Rogachevskii and Kleeorin, 2007; Brandenburg, Kleeorin, and Rogachevskii, 2010; Brandenburg *et al.*, 2011) as a possible mechanism for producing magnetic-flux concentrations of the form of active regions. Of course a magnetic field [$\boldsymbol{B}$] always gives rise to a positive magnetic pressure [$\boldsymbol{B}^2/2\mu_0$], where μ_0 is the vacuum permeability. In a turbulent medium, however, magnetic fields also suppress the turbulence and thus decrease the turbulent pressure [$\rho\boldsymbol{u}^2/3$], and modify the pressure caused by magnetic fluctuations [$\boldsymbol{b}^2/6\mu_0$]. Here, $\boldsymbol{u}$ and $\boldsymbol{b}$ are velocity and magnetic fluctuations, ρ is the density, μ_0 is the vacuum permeability, and the coefficients in the turbulent fluid and magnetic pressure are given for isotropic turbulence. Magnetic fluctuations can be due to both small-scale dynamo action as well as tangling of a large-scale field [$\overline{\boldsymbol{B}}$]. The total field is thus $\boldsymbol{B} = \overline{\boldsymbol{B}} + \boldsymbol{b}$. The sum of both effects [$p_{\text{turb}} = \overline{\rho\boldsymbol{u}^2}/3 + \overline{\boldsymbol{b}^2}/6\mu_0$] is positive definite, but it depends on $\overline{\boldsymbol{B}}$, and p_{turb} tends to be reduced as $\overline{B} \equiv |\overline{\boldsymbol{B}}|$ increases. Indeed, $p_{\text{turb}} = 2E_T/3 - \overline{\boldsymbol{b}^2}/6\mu_0$, where the total turbulent energy $E_T = \overline{\rho\boldsymbol{u}^2}/2 + \overline{\boldsymbol{b}^2}/2\mu_0 \approx$ constant, so that the change of the turbulent pressure is negative ($\delta p_{\text{turb}} < 0$) when the magnetic fluctuations are generated by tangling of the mean magnetic field by the velocity fluctuations at the expense of turbulent kinetic energy (Kleeorin, Rogachevskii, and Ruzmaikin, 1990; Brandenburg *et al.*, 2011). Thus, we write

$$p_{\text{turb}}(\overline{B}) = p_{\text{turb}}(0) - q_{\text{p}}(\overline{B})\,\overline{B}^2/2\mu_0, \qquad (1)$$

where $p_{\text{turb}}(0)$ is the turbulent pressure at zero mean field and $q_{\text{p}}(\overline{B})$ is a positive function of $\overline{B}$ such that p_{turb} is reduced in the presence of $\overline{B}$. The pressure $p_{\text{turb}}(0)$ only includes those contributions from $\boldsymbol{b}^2$ that are associated with small-scale dynamo action, but not the magnetic fluctuations resulting from the tangling of the mean magnetic field. The relevant magnetic pressure in the evolution equation for the mean flow [$\overline{\boldsymbol{U}}$] is then not just $\overline{B}^2/2\mu_0$, but it is affected by the $\overline{B}$-dependence of p_{turb}, *i.e.* it depends on

$$p_{\text{turb}}(\overline{B}) + \overline{B}^2/2\mu_0 = p_{\text{turb}}(0) + \left[1 - q_{\text{p}}(\overline{B})\right]\overline{B}^2/2\mu_0, \qquad (2)$$

which is also still positive. But $1 - q_{\text{p}}(\overline{B})$ may well become negative, which leads to what we call a *negative effective magnetic pressure*. The first term, $p_{\text{turb}}(0)$, on the right-hand side of Equation (2) is independent of $\overline{B}$, so it ignores the dynamics of the mean field and only affects the density scale height. Therefore, the expression

$$p_{\text{eff}} = (1 - q_{\text{p}})\overline{B}^2/2\mu_0 \qquad (3)$$

is referred to as the *effective* magnetic pressure. We emphasize that the effective magnetic pressure is an averaged quantity describing the dependence on the mean magnetic field. One

could therefore also talk about a magnetic mean-field pressure. In addition, there is also the gas pressure [p_{gas}]. Once the effective magnetic pressure drives a mean flow, the gas density changes, and as a consequence the gas pressure, so as to re-establish approximate total pressure balance. Therefore, p_{gas} and ρ will also depend on $\overline{B}$.

In the presence of gravity, the properties of magnetic buoyancy are drastically altered by a negative effective magnetic pressure. In the following we illustrate how this can lead to an instability. Since the flow velocities are highly subsonic, we can make the anelastic approximation, *i.e.* $\nabla \cdot \overline{\rho U} = 0$. This leads to $\nabla \cdot \overline{U} + \overline{U} \cdot \nabla \ln \overline{\rho} = 0$, or

$$\nabla \cdot \overline{U} = \frac{\overline{U}_z}{H_\rho}, \tag{4}$$

where we have used the density scale height [H_ρ], so that $\nabla \ln \overline{\rho} = (0, 0, -1/H_\rho)$. This equation shows that a downward motion, $\overline{U}_z < 0$, leads to compression: $\nabla \cdot \overline{U} < 0$. This enhances an applied field locally. We consider an applied equilibrium magnetic field of the form $(0, B_0, 0)$ and the mean field has only a y-component, *i.e.* $\overline{B} = (0, \overline{B}_y(x, z), 0)$, so we have

$$\frac{D\overline{B}_y}{Dt} = -\overline{B}_y \nabla \cdot \overline{U}, \tag{5}$$

where $D/Dt = \partial/\partial + \overline{U} \cdot \nabla$ is the advective derivative. Note that for a magnetic field with only a y-component, but $\partial/\partial y = 0$, there is no stretching term, so there is no term of the form $\overline{B} \cdot \nabla \overline{U}$. Using Equation (4), and linearizing Equation (5) around $\overline{U} = \mathbf{0}$ and $\overline{B} = B_0$, we have

$$\frac{\partial \overline{B}_{1y}}{\partial t} = -B_0 \frac{\overline{U}_{1z}}{H_\rho}, \tag{6}$$

where subscripts 1 denote linearized quantities. The vertical-velocity perturbation [$\overline{U}_{1z}$] is caused by magnetic buoyancy. Assuming total pressure equilibrium, $p_{gas} + p_{eff} = $ constant, we see that an increase in the effective magnetic pressure causes a *decrease* is the gas pressure, *i.e.* $\delta p_{gas} = -\delta p_{eff}$, just as in the regular magnetic-buoyancy instability. Therefore, the Archimedian buoyancy force is

$$-\frac{\delta \rho}{\rho} g = -\frac{\delta p_{gas}}{p_{gas}} g = \frac{\delta p_{eff}}{\rho c_s^2} g = \frac{dp_{eff}}{d\overline{B}^2} \frac{\delta \overline{B}^2}{\rho c_s^2} g, \tag{7}$$

where we have used $p_{gas} = \rho c_s^2$ for an isothermal gas. In the regular magnetic-buoyancy instability (Parker, 1966, 1979), without turbulence effects, we have $2\mu_0 \, dp_{eff}/d\overline{B}^2 = 1$. In the domain where the negative effective magnetic-pressure effect causes $dp_{eff}/d\overline{B}^2$ to be negative, a magnetic-field enhancement leads to a further reduction of the local pressure, which is compensated by horizontal inflows, increasing density (and field strength), making this fluid parcel heavier, causing it to sink. Conversely, a local field reduction causes outflows and rises until it reaches the region where this feedback reverses. Thus, the instability loop is closed by considering the momentum equation in its linearized form:

$$\frac{\partial \overline{U}_{1z}}{\partial t} = \frac{dp_{eff}}{d\overline{B}^2} \frac{2B_0 \overline{B}_{1y}}{\rho c_s^2} g. \tag{8}$$

Using $c_s^2/g = H_\rho$ for an isothermal atmosphere, we then find the dispersion relation for the growth rate [λ] of the resulting instability

$$\lambda = \frac{v_A}{H_\rho} \sqrt{-2\mu_0 \, p'_{eff}} - \eta_t k^2, \tag{9}$$

where $v_A = B_0/\sqrt{\mu_0\rho}$ is the Alfvén speed and

$$2\mu_0\,p'_{\text{eff}} = 2\mu_0\,\mathrm{d}p_{\text{eff}}/\mathrm{d}\overline{B}^2 = 1 - q_p - \mathrm{d}q_p/\mathrm{d}\ln\overline{B}^2 \tag{10}$$

is twice the derivative of the effective magnetic pressure. We have also included here the effects of turbulent magnetic diffusivity [η_t] and turbulent magnetic viscosity [ν_t], assuming $\nu_t/\eta_t = 1$. Here, k is the effective wavenumber. A proper derivation of the growth rate of the instability, but again without including turbulent magnetic diffusivity and turbulent magnetic viscosity, is given in Appendix A. This analysis shows that the first term in Equation (9) is to be multiplied by a factor k_x/k, as is also familiar for gravity modes (Stein and Leibacher, 1974). This implies that $\lambda = 0$ for $k_x = 0$, and that $\lambda(k_x)$ has a maximum for intermediate values of k_x; see Appendix A.

The negative contribution of turbulence to the mean magnetic pressure and the resulting large-scale instability has been predicted long ago (Kleeorin, Rogachevskii, and Ruzmaikin, 1990; Kleeorin, Mond, and Rogachevskii, 1996; Kleeorin and Rogachevskii, 1994). However, this instability has been detected in direct numerical simulations (DNS) only recently (Brandenburg *et al.*, 2011; Kemel *et al.*, 2012a). This large-scale instability is called the negative effective magnetic pressure instability (NEMPI).

Equation (9) demonstrates that stronger stratification and thus a smaller scale height leads to an increased growth rate of the instability. This was qualitatively confirmed by Kemel *et al.* (2012b). Using numerical solutions of the full mean-field equations, they found furthermore that the growth rate of the instability is actually independent of v_A. This seems to be at odds with Equation (9). To understand this, we use the following approximation for q_p, based on fits to the DNS results (Brandenburg *et al.*, 2011, 2012; Kemel *et al.*, 2012b):

$$q_p(\beta) = \frac{\beta_\star^2}{\beta_p^2 + \beta^2}, \tag{11}$$

where $\beta_\star$ and β_p are constants, $\beta = \overline{B}/B_{\text{eq}}$ is the modulus of the normalized mean magnetic field, and $B_{\text{eq}} = \sqrt{\mu_0\rho}u_{\text{rms}}$ is the equipartition field strength. Thus, for $\beta_\star \gg \beta \gg \beta_p$, we have

$$\lambda \approx \beta_\star \frac{u_{\text{rms}}}{H_\rho} - \eta_t k^2, \tag{12}$$

so the growth rate is indeed independent of the imposed field strength.

In a mean-field model, u_{rms} is normally expressed in terms of $\eta_t = u_{\text{rms}}/3k_f$, where k_f is the wavenumber of the energy-carrying eddies, so Equation (12) becomes

$$\frac{\lambda}{\eta_t k^2} \approx 3\beta_\star \frac{k_f/k}{kH_\rho} - 1, \tag{13}$$

which illustrates immediately the importance of large enough scale separation, *i.e.* large enough values of k_f/k.

The purpose of this article is to show that NEMPI can work over a range of different field strengths. Such a result was recently predicted using the mean-field simulations (MFS) by Kemel *et al.* (2012b). We shall also investigate the close connection between MFS and DNS results, which allows us to determine the resulting effective magnetic pressure as a function of the mean magnetic field in the plane perpendicular to the mean field. Here we focus on a series of simulations with different field strengths, but for a fixed value of the magnetic Reynolds number and fixed value of the scale separation ratio. For a numerical study of the dependence on magnetic Reynolds number and on scale separation ratio, but fixed field strength, we refer to the recent work of Kemel *et al.* (2012a). In the following, we discuss first DNS of NEMPI and turn then to MFS. We begin with a simplistic illustration of the nature of NEMPI.

2. Vertical Profile of Effective Magnetic Pressure

The first successful DNS of NEMPI has been possible under the assumption of an isother-
mally stratified layer with an isothermal equation of state (Brandenburg *et al.*, 2011). Much
of the same physics is also possible in adiabatically stratified layers, but NEMPI was found
in this case only in mean-field models (Brandenburg, Kleeorin, and Rogachevskii, 2010;
Käpylä *et al.*, 2012). The isothermal case has conceptual advantages that help us understand
better the underlying physics of this instability. We make use of this advantage in the present
article, too.

In most of the isothermal setups studied so far, the rms velocity is only weakly dependent
on height, so the z-variation of B_{eq} was only caused by that of $\rho = \rho_0 \exp(-z/H_\rho)$. Before
we perform DNS and MFS, let us determine the conditions for which NEMPI is most effec-
tive. To this end we plot the effective magnetic pressure, which is normalized by the local
equipartition field strength [B_{eq}],

$$\mathcal{P}_{eff}(\beta) = \frac{1}{2}\big[1 - q_p(\beta)\big]\beta^2, \tag{14}$$

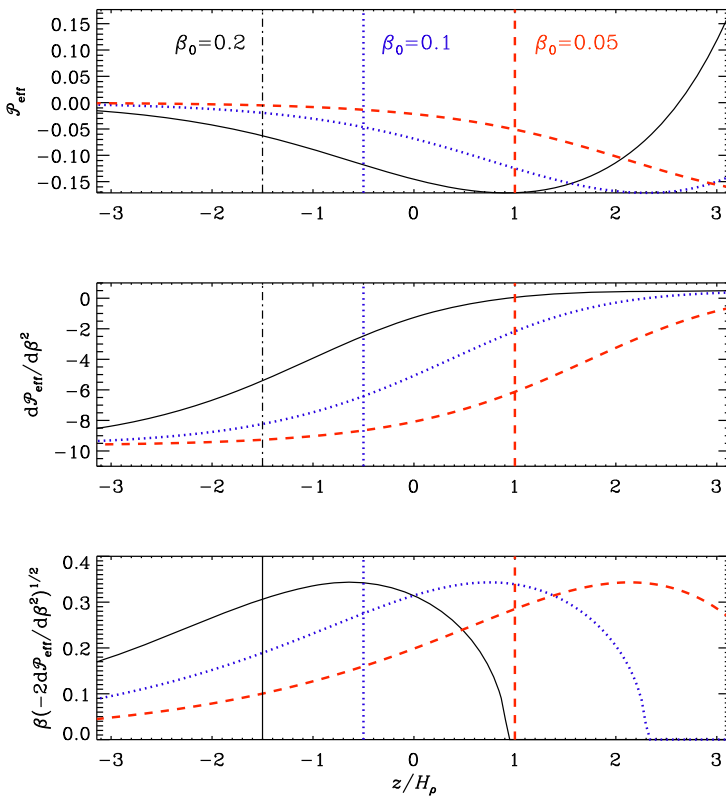**Figure 1** Profiles of $\mathcal{P}_{eff}$, $d\mathcal{P}_{eff}/d\beta^2$, and $\beta(-2d\mathcal{P}_{eff}/d\beta^2)^{1/2}$ for fit parameters $q_{p0} = 20$ and $\beta_p = 0.167$,
and the three field strengths $B_0/B_{eq0} = 0.05$, 0.1, and 0.2 within the z-range from $-\pi$ to π, which is consis-
tent with some of the models discussed below. The vertical lines of similar line types give the location where
the unstable eigenmodes reaches its peak.

i.e. $\mathcal{P}_{\text{eff}} = p_{\text{eff}}/B_{\text{eq}}^2$, where $q_{\text{p}}(\beta)$ is determined by Equation (11). Since $\beta = \beta(z) = \beta_0 \exp(z/2H_\rho)$ increases with z, $\mathcal{P}_{\text{eff}}(z)$ is small at large depths, reaches a negative minimum at some depth, and then becomes positive and equal to β^2. In Figure 1 we show vertical profiles of $\mathcal{P}_{\text{eff}}$, $\mathrm{d}\mathcal{P}_{\text{eff}}/\mathrm{d}\beta^2$, and $\beta(-2\mathrm{d}\mathcal{P}_{\text{eff}}/\mathrm{d}\beta^2)^{1/2}$ for the fit parameters $q_{\text{p}0} = 20$ and $\beta_{\text{p}} = 0.167$ derived later in this article, and the three field strengths $\beta_0 \equiv B_0/B_{\text{eq}0} = 0.05$, 0.1, and 0.2 within the z/H_ρ-range from $-\pi$ to π, which is also consistent with the DNS and some of the MFS discussed below. Here, $B_{\text{eq}0} = B_{\text{eq}}(z = 0)$, $q_{\text{p}0} = q_{\text{p}}(\beta = 0)$, and $\beta_\star = \beta_{\text{p}}\sqrt{q_{\text{p}0}}$.

Notice first of all that all three curves of $\mathcal{P}_{\text{eff}}$ have minima with left flanks (negative slopes) within the domain. As the imposed field is increased, these curves shift downward (smaller values of z). Thus, we should expect the peak of the unstable eigenmode to appear somewhere along the left flanks of these curves and that these peaks move further down as the imposed field is increased. This is qualitatively reproduced by the DNS and MFS discussed below, except that the location is consistently a certain distance below the position where the left flanks have their steepest gradient. On the other hand, as is evident from the middle panel of Figure 1, the largest value of $\mathrm{d}\mathcal{P}_{\text{eff}}/\mathrm{d}\beta^2$ is always achieved at the bottom of the domain. However, the growth rate of NEMPI still has a factor proportional to $v_{\text{A}} = u_{\text{rms}}\beta$ in front of it; see Equation (9). This then confines the instability to a narrow strip within the domain. In the third panel of Figure 1 we also plot therefore $\beta(-2\mathrm{d}\mathcal{P}_{\text{eff}}/\mathrm{d}\beta^2)^{1/2}$, and their extrema are now only slightly above the location where DNS and MFS show a peak in the eigenfunction. The reason for the remaining discrepancy is not well understood at present.

3. Onset and Saturation of NEMPI in DNS

3.1. Isothermal Setup in DNS

Following the earlier work of Brandenburg *et al.* (2011) and Kemel *et al.* (2012a), we solve the equations for the velocity [U], the magnetic vector potential [A], and the density [ρ]:

$$\rho\frac{\mathrm{D}U}{\mathrm{D}t} = -c_{\text{s}}^2\nabla\rho + J \times B + \rho(f + g) + \nabla \cdot (2\nu\rho\mathsf{S}), \tag{15}$$

$$\frac{\partial A}{\partial t} = U \times B + \eta\nabla^2 A, \tag{16}$$

$$\frac{\partial\rho}{\partial t} = -\nabla \cdot \rho U, \tag{17}$$

where ν is the kinematic viscosity, η is the magnetic diffusivity due to Spitzer conductivity of the plasma, $B = B_0 + \nabla \times A$ is the magnetic field, $B_0 = (0, B_0, 0)$ is the imposed uniform field, $J = \nabla \times B/\mu_0$ is the current density, μ_0 is the vacuum permeability, $\mathsf{S}_{ij} = \frac{1}{2}(\partial_j U_i + \partial_i U_j) - \frac{1}{3}\delta_{ij}\nabla \cdot U$ is the traceless rate-of-strain tensor. The forcing function [f] consists of random, white-in-time, plane, non-polarized waves with a certain average wavenumber [k_{f}]. The turbulent rms velocity is approximately independent of z with $u_{\text{rms}} = \langle u^2\rangle^{1/2} \approx 0.1\,c_{\text{s}}$. The gravitational acceleration [$g = (0, 0, -g)$] is chosen such that $k_1 H_\rho = 1$, so the density contrast between bottom and top is $\exp(2\pi) \approx 535$. Here, $H_\rho = c_{\text{s}}^2/g$ is the density scale height and $k_1 = 2\pi/L$ is the smallest wavenumber that fits into the cubic domain of size L^3. In most of our calculations, structures develop whose horizontal wavenumber [k_x] is close to k_1. We consider a domain of size $L_x \times L_y \times L_z$ in Cartesian coordinates (x, y, z), with periodic boundary conditions in the x- and y-directions and stress-free, perfectly conducting boundaries at the top and bottom ($z = \pm L_z/2$). In all

cases, we use a scale separation ratio $[k_f/k_1]$ of 30, a fluid Reynolds number $\mathrm{Re} \equiv u_{rms}/\nu k_f$ of 18, and a magnetic Prandtl number $[\mathrm{Pr}_M = \nu/\eta]$ of 0.5. In our units, $\mu_0 = 1$ and $c_s = 1$. The value of B_0 is specified in units of the volume-averaged value $[B_{eq0} = \sqrt{\mu_0 \rho_0} \, u_{rms}]$ where $\rho_0 = \langle \rho \rangle$ is the volume-averaged density, which is constant in time. In addition to visualizations of the actual magnetic field, we also monitor $\overline{B}_y$, which is an average over y and a certain time interval $[\Delta t]$. Time is sometimes specified in terms of turbulent-diffusive times $[t \, \eta_{t0} k_1^2]$, where $\eta_{t0} = u_{rms}/3k_f$ is the estimated turbulent diffusivity. Since the simulations are periodic in the x- and y-directions, we sometimes shift the images such that the peak field strength of NEMPI appears in the middle of the frame.

The simulations are performed with the PENCIL CODE [http://pencil-code.googlecode.com] which uses sixth-order explicit finite differences in space and a third-order accurate time stepping method. We use a numerical resolution of 256^3 mesh points.

3.2. Results

In Figure 2 we demonstrate that NEMPI can work over a range of field strengths. As we increase the strength of the imposed field, NEMPI develops at progressively greater depth. This result was recently obtained for MFS, but is now for the first time demonstrated in DNS. Figure 3 shows that the growth of the large-scale field $[\overline{B}_1]$ of the magnetic structure is similar for three different field strengths. Here, $\overline{B}_1$ has been determined by taking the maximum value of the mean field in the neighborhood of the position where the flux concentration later develops. Note that there is a range over which $\overline{B}_1$ grows approximately exponentially, independent of the value of B_0.

In Figure 4 we show $\overline{B}_y$ at early, intermediate, and late stages of the saturation process (left), and compare with visualizations of $\mathcal{P}_{eff}$ at the same times. Here, $\mathcal{P}_{eff} = \frac{1}{2}(1 - q_p)\beta^2$, where $q_p(\beta)$ with $\beta = \overline{B}/B_{eq}$ is evaluated from

$$q_p = -2\Delta\overline{\Pi}_{xx}^f / \overline{B}^2, \tag{18}$$

for $\boldsymbol{B}_0 = (0, B_0, 0)$, and

$$\Delta\overline{\Pi}_{ii}^f = \overline{\rho}\left(\overline{u_i^2} - \overline{u_{0i}^2}\right) + \frac{1}{2}\left(\overline{\boldsymbol{b}^2} - \overline{\boldsymbol{b}_0^2}\right) - \left(\overline{b_i^2} - \overline{b_{0i}^2}\right), \tag{19}$$

is applied to the xx-component of the total stress from the fluctuating velocity and magnetic fields. In Equation (19) no summation over the repeated index i is assumed.

In Figure 4, blue shades correspond to low values of $\mathcal{P}_{eff}$ and occur around the minimum line (marked in white) where $\mathcal{P}_{eff} = \mathcal{P}_{min}$. As time progresses, low values of $\mathcal{P}_{eff}$ are also found at greater depth as the magnetic-flux concentration descends. The fact that there is a clear spatial correlation between $\overline{B}_y$ and $\mathcal{P}_{eff}$ provides strong evidence that the interpretation of the formation of structures in the stratified turbulence simulations in terms of NEMPI is indeed the correct one.

The descending structures have previously been referred to as "potato sack" structures (Brandenburg *et al.*, 2011), because of their widening cross-section with greater depth. When such structures were first seen in MFS (Brandenburg, Kleeorin, and Rogachevskii, 2010), they were originally thought to be artifacts of the model that one would not expect to see in the Sun. However, such structures were later also found in DNS (Brandenburg *et al.*, 2011), highlighting therefore the strong predictive power of MFS.

A visualization of the resulting mean flow $[\overline{U}]$ is shown in Figure 5 as vectors. The flow shows a convergent shape toward the magnetic structures. It is interesting to note that such convergent flow structures are now also seen in local-helioseismic flow measurements
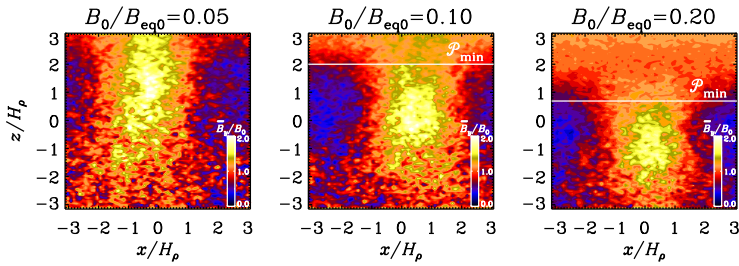
Figure 2 $\overline{B}_y/B_0$ from DNS for three values of the imposed field strength at the end of the linear growth phase of NEMPI for $\mathrm{Re}_M = 18$ and $\mathrm{Pr}_M = 0.5$. The times are $t\,\eta_{t0}/H_\rho^2 \approx 0.93$, 1.09, and 1.26 for $B_0/B_{eq0} = 0.05$, 0.1, and 0.2, respectively. The location of the $\mathcal{P}_{\min}$ line is indicated in panels 2 and 3, while for panel 1 it lies above the computational domain.
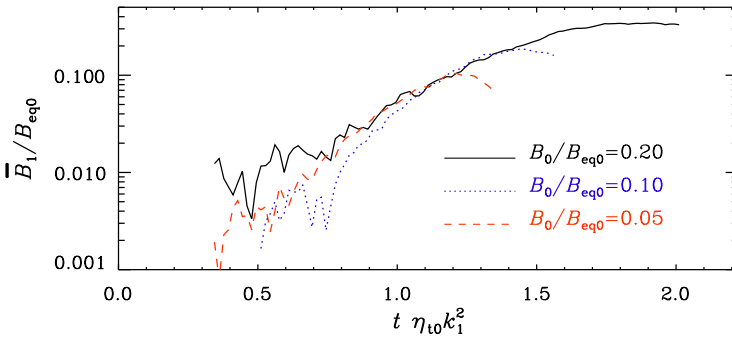

Figure 3 Growth of the large-scale field strength $[\overline{B}_1]$ at the center of the magnetic structure for three field strengths.

around active regions (Hindman, Haber, and Toomre, 2009). In this connection it is instructive to discuss the somewhat peculiar shape of such a structure that widens as it descends. Normally, in a strongly stratified atmosphere, descending structures get compressed and become narrower, but this is not seen in the present visualizations. As already argued by Brandenburg *et al.* (2012), this is because the boundaries of these structures do not coincide with material lines, so the mass is not conserved inside them and can leak through the boundaries. Indeed, these structures grow as they descend, and may become amenable to helioseismic detection; *cf.* Ilonidis, Zhao, and Kosovichev (2011). This phenomenon is well known in the description of turbulent plumes as a model of turbulent downdrafts in convection (Rieutord and Zahn, 1995). Such structures are known to widen as a result of entrainment. The sinking behavior of these apparently disconnected flow structures can be explained as follows: while inflows dominate downflows throughout the whole lifespan of the field concentration, in the initial stage the former can drag in a large fraction of the surrounding magnetic field, overcompensating the losses by downflows. However, as the environment gets depleted, this dynamical balance shifts and the structures start moving downwards.

3.3. Mean-Field Coefficients from DNS

In earlier work by Kemel *et al.* (2012b), the parameters $q_{p0} = 40$ and $\beta_p = 0.05$, corresponding to $\beta_\star = 0.32$, were used. Those values are compatible with work by Brandenburg *et al.*
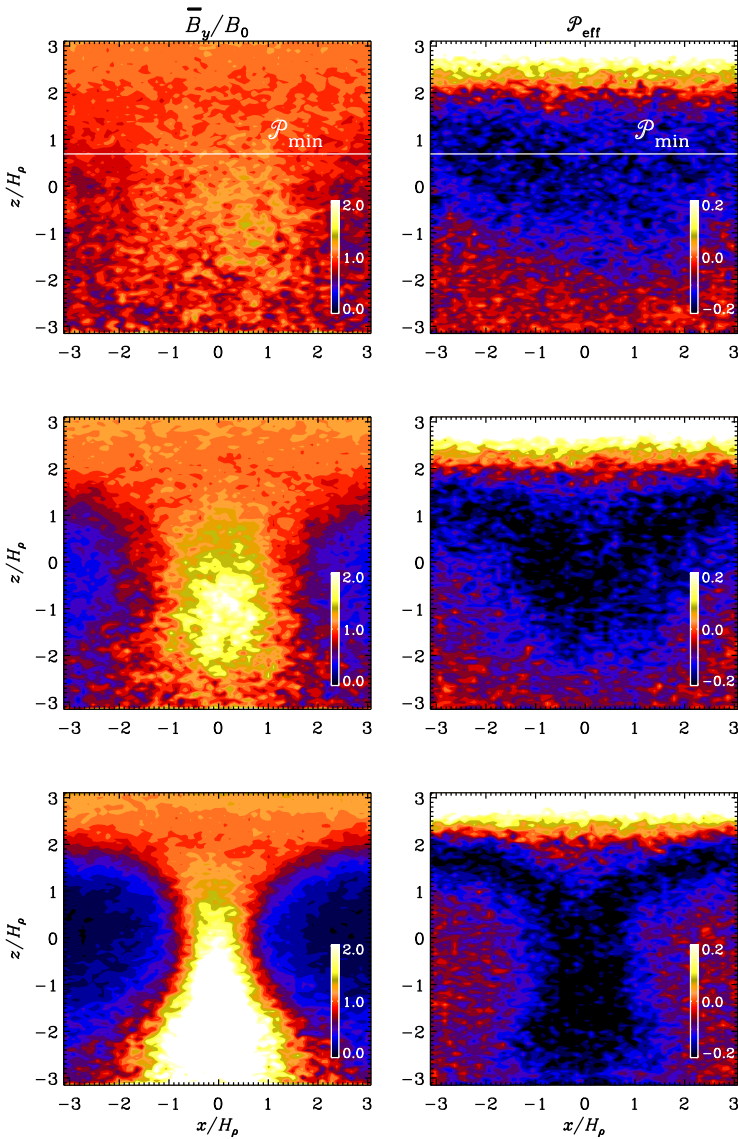
Figure 4 $\overline{B}_y$ and $\mathcal{P}_{\text{eff}}$ from DNS at three times ($t\,\eta_{t0}/H_\rho^2 \approx 0.84$, 1.34 and 1.84) showing the descent of the potato sack feature for $\text{Re}_M = 18$, $\text{Pr}_M = 0.5$, and $B_0/B_{\text{eq0}} = 0.20$.

(2012) and Kemel *et al.* (2012a). However, in the present case we have a larger scale separation ratio, $k_{\text{f}}/k_1 = 30$, for which these parameters have not yet been determined. In Figure 6 we show the functional form of $\mathcal{P}_{\text{eff}}(\beta)$ for the present case with $k_{\text{f}}/k_1 = 30$, $\text{Re}_M = 18$, and $\text{Pr}_M = 0.5$. Here we have followed the method described by Brandenburg *et al.* (2012); see their Equation (17). For the present model we find as fit parameters $q_{\text{p0}} = 20$ and $\beta_{\text{p}} = 0.167$, which corresponds to $\beta_\star = 0.75$.

Figure 5 Vectors of $\overline{U}$ together with a color/grey-scale representation of $\overline{B}_y$ from DNS at a late time ($t\,\eta_{t0}/H_\rho^2 \approx 1.7$) for $\mathrm{Re}_M = 18$, $\mathrm{Pr}_M = 0.5$, and $B_0/B_{\mathrm{eq0}} = 0.20$. The color scale is the same as in the lower left panel of Figure 4, and the longest vector corresponds to a flow speed of $0.04c_s$ or $0.4u_{\mathrm{rms}}$.
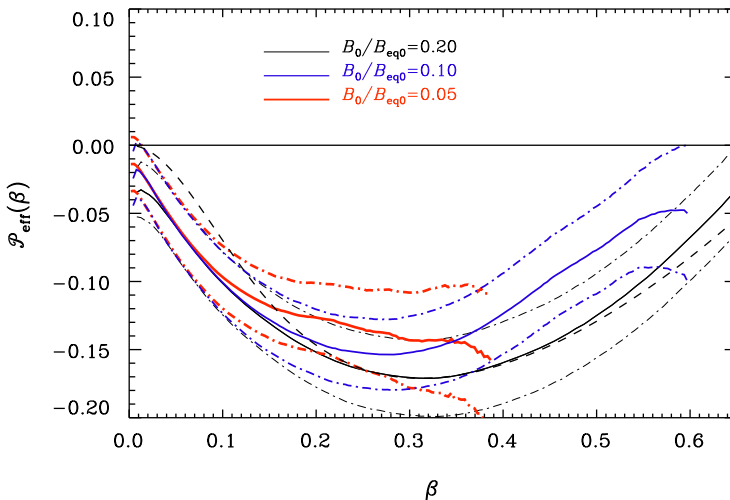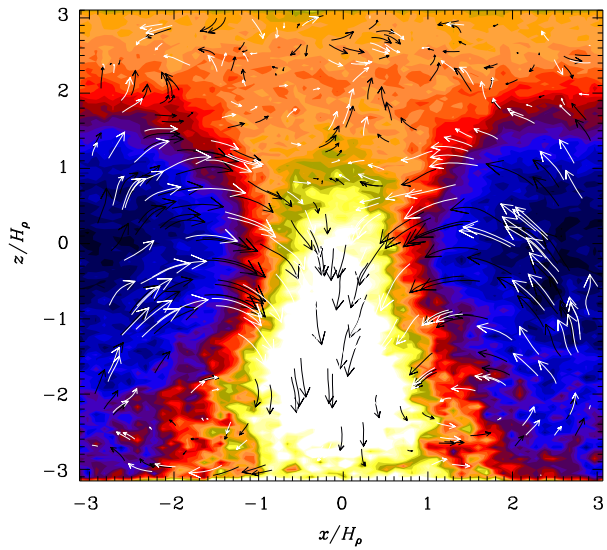

Figure 6 $\mathcal{P}_{\mathrm{eff}}(\beta)$ for the DNS used in this article with $k_{\mathrm{f}}/k_1 = 30$, $\mathrm{Re}_M = 18$, and $\mathrm{Pr}_M = 0.5$. The dashed line is a fit based on Equation (11) with $q_{\mathrm{p0}} = 20$ and $\beta_{\mathrm{p}} = 0.167$, which corresponds to $\beta_\star = 0.75$, and the dashed-dotted lines show the error-bar range.

4. Comparison with MFS

Recently, many aspects of NEMPI seen in the DNS have also been detected in MFS. Establishing the usefulness and limitations of MFS is important, because such models are easier to solve and allow one to explore parameters in regimes where DNS are harder to apply or have not yet been applied in the limited time since the close correspondence between DNS and MFS was first noted.

In the following we consider two-dimensional mean-field models, in which the presence of q_s has no effect on the solutions (Kemel *et al.*, 2012b). Furthermore, we ignore other

effects connected with the anisotropy of the turbulence. These effects have previously been found to be weak (Brandenburg *et al.*, 2012; Käpylä *et al.*, 2012).

4.1. Isothermal Setup in MFS

In this section we solve the evolution equations for mean velocity $\overline{U}$, mean density $\overline{\rho}$, and mean vector potential $\overline{A}$, in the form

$$\frac{\partial \overline{U}}{\partial t} = -\overline{U} \cdot \nabla \overline{U} - c_s^2 \nabla \ln \overline{\rho} + \boldsymbol{g} + \overline{\mathcal{F}}_M + \overline{\mathcal{F}}_K, \tag{20}$$

$$\frac{\partial \overline{\rho}}{\partial t} = -\overline{U} \cdot \nabla \overline{\rho} - \overline{\rho} \nabla \cdot \overline{U}, \tag{21}$$

$$\frac{\partial \overline{A}}{\partial t} = \overline{U} \times \overline{B} - (\eta_t + \eta)\overline{J}, \tag{22}$$

where $\overline{\mathcal{F}}_M$ is given by

$$\overline{\rho} \overline{\mathcal{F}}_M = -\frac{1}{2} \nabla \left[(1 - q_p) \overline{B}^2 \right], \tag{23}$$

and

$$\overline{\mathcal{F}}_K = (\nu_t + \nu) \left(\nabla^2 \overline{U} + \frac{1}{3} \nabla \nabla \cdot \overline{U} + 2\overline{\mathsf{S}} \nabla \ln \overline{\rho} \right) \tag{24}$$

is the total (turbulent plus microscopic) viscous force. Here, $\overline{\mathsf{S}}_{ij} = \frac{1}{2}(\overline{U}_{i,j} + \overline{U}_{j,i}) - \frac{1}{3}\delta_{ij} \nabla \cdot \overline{U}$ is the traceless rate-of-strain tensor of the mean flow and q_p is approximated by Equation (11), which is only a function of the ratio $\beta \equiv |\overline{B}|/B_{eq}$. In Equation (23) we have taken into account that the mean magnetic is independent of y, so the mean magnetic tension vanishes.

4.2. Aspects of the MFS

We begin by showing $\overline{B}_y$ for three values of the imposed field strength at the end of the linear growth phase of NEMPI. The results are shown in Figures 7 and 8 for two different setups. In the former we use $q_{p0} = 20$ and $\beta_p = 0.167$ for the same z-range ($-\pi \leq z/H_\rho \leq \pi$) as in the DNS, while in the latter we use $q_{p0} = 40$ and $\beta_p = 0.05$ for somewhat stronger fields and a deeper z-range ($0 \leq z/H_\rho \leq 2\pi$), which is also the fiducial model used by Kemel *et al.* (2012b). In the former case the growth rate is $\approx 11 H_\rho^2/\eta_t$, while in the latter it is $\approx 5.0 H_\rho^2/\eta_t$.

Unlike the DNS, the MFS show that in the former series of models with $q_{p0} = 20$ and $\beta_p = 0.167$ the x-extent is slightly larger than the optimal horizontal wavelength of the instability, because one sees that some of the structures begin to split into two (Figure 7). This is not the case for the second model with $q_{p0} = 40$ and $\beta_p = 0.05$ (Figure 8).

Next, we compare $\overline{B}_y$ with $\mathcal{P}_{eff} = \frac{1}{2}(1 - q_p)\beta^2$. Again, there is a close correspondence between the $\overline{B}_y$ field and the resulting distribution of $\mathcal{P}_{eff}$; see Figure 9. Here, $q_p(\beta)$ is evaluated using Equation (11). Furthermore, there is a close correspondence between regions of enhanced magnetic field and enhanced density; see the right-most column of Figure 9. Note also that the relative variation of the mean density $[\Delta\overline{\rho}/\overline{\rho}]$ is of the order of 10^{-4}. This small value is a consequence of the plasma β being very large, *i.e.* $\overline{B}^2/2\mu_0\overline{\rho}c_s^2 \ll 1$. Indeed, we expect $\Delta\overline{\rho}/\overline{\rho} \approx \overline{B}^2/2\mu_0\rho c_s^2 = \beta^2 M_a^2$, where β at $z/H_\rho = -5$ is about 0.1 and $M_a = u_{rms}/c_s$ is the rms Mach number, which is also about 0.1. We note that similar values are also seen in DNS, but here the variations from the turbulence are typically much larger.
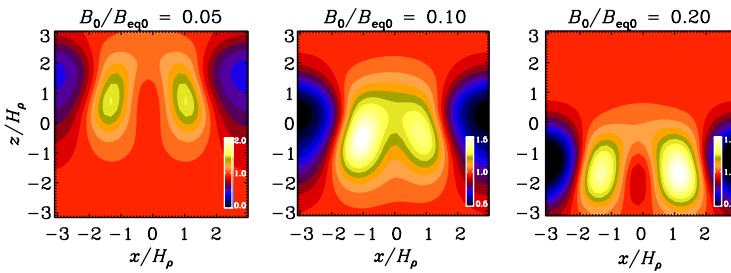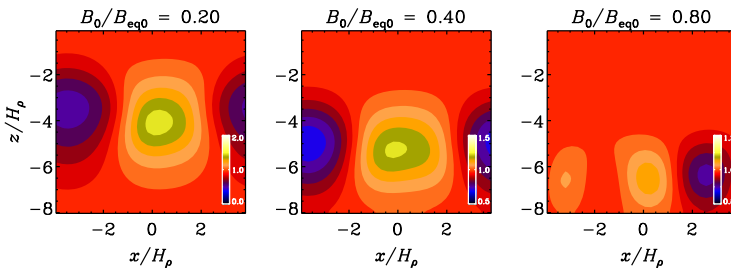
Figure 7 $\overline{B}_y/B_0$ from mean-field models for three values of the imposed field strength at the end of the linear growth phase of NEMPI. Here, $q_{p0} = 20$ and $\beta_p = 0.167$, which corresponds to $\beta_\star = 0.75$. The times are $t\,\eta_t/H_\rho^2 \approx 0.84$, 0.99, and 1.14 for $B_0/B_{eq0} = 0.05$, 0.1, and 0.2, respectively.

Figure 8 $\overline{B}_y/B_0$ from mean-field models for three values of the imposed field strength at the end of the linear growth phase of NEMPI, but for larger field strengths than in Figure 7 and vertical domain boundaries that are deeper down, so the magnetic field maxima of the instability fit better into the domain. Here, $q_{p0} = 40$ and $\beta_p = 0.05$, corresponding to $\beta_\star = 0.32$.

5. Application to the Sun

The motivation for studying an isothermal model lies in its simplicity, allowing a more thorough investigation of all possible aspects of NEMPI. The Sun is obviously not isothermal nor is it stably stratified. The purpose of this section is to discuss what is known about model dependencies of NEMPI and what else can be learn from the isothermal model. We here discuss the aspects of stratification, scale separation, and the combination of both.

i) *Stratification.* As we have shown above, NEMPI requires strong stratification: decreasing H_ρ increases the growth rate; see Equation (13). The restoring force associated with stable stratification gives rise to Brunt–Väisälä oscillations, which are however eliminated by using an isothermal equation of state. Including it tends to suppress NEMPI, as was shown by Käpylä *et al.* (2012). In an isentropic layer with marginal stability, this stabilizing effect is absent. The temperature increases now linearly with depth. The scale height is then smallest near the top, so NEMPI always tends to develop in the upper layers. Nevertheless, unstable structures still sink; see Brandenburg, Kleeorin, and Rogachevskii (2010).

ii) *Scale separation.* The growth rate increases with the scale separation ratio; see Equation (13). This suppresses NEMPI in deeper layers, so sinking structures must eventually dissolve. Such a variable scale-separation ratio is not yet included in our model. Realistic models of solar convection, such as those of Kitiashvili *et al.* (2010) or Stein *et al.* (2011), may not have enough scale separation; in our models we used $k_f/k_1 = 30$. Also, it is important that the models are run for long enough; see the discussion in Kemel *et al.* (2012a).
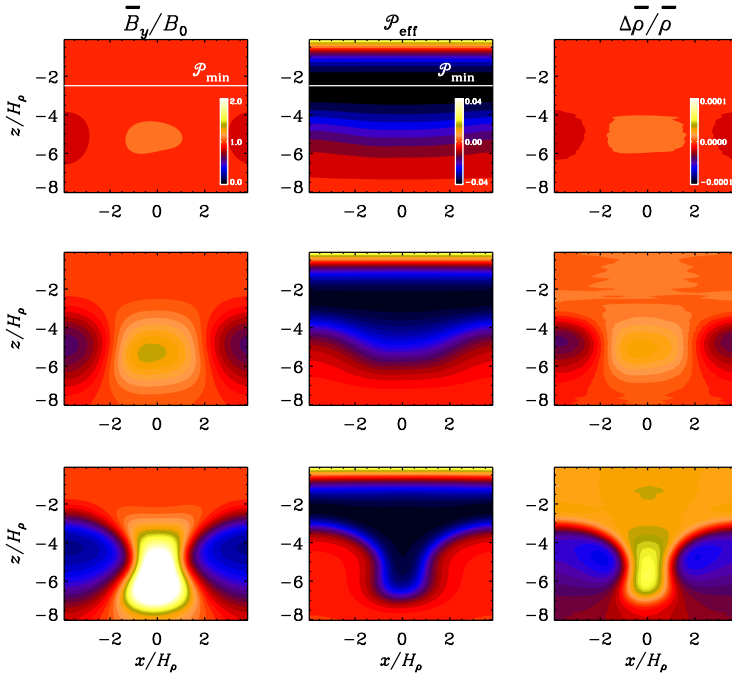
Figure 9 $\overline{B}_y/B_0$, $\mathcal{P}_{\mathrm{eff}}$, and $\Delta\overline{\rho}/\overline{\rho}$ from mean-field models at three times: $t\,\eta_{\mathrm{t}}/H_\rho^2 \approx 2.2$, 2.5, and 2.8. Here, $B_0/B_{\mathrm{eq}0} = 0.40$.

iii) *Relation between stratification and scale separation.* In the model we have varied H_ρ and k_{f} separately, but in the Sun the scale of the turbulent eddies is believed to be proportional to the local scale height, so $k_{\mathrm{f}}H_\rho \approx$ constant. Furthermore, in an isothermal domain, the value of k_1 has no physical significance, because the solution is independent of the position of the boundaries provided they are sufficiently far away from the location where the large-scale structures develop. In most of the models presented above, k_1 was equal to the horizontal wavenumber $[k_x]$ of the structures. In Figure 10 we show that, as we decrease H_ρ by a factor of three, the horizontal wavelength also decreases by a factor of three, and so $k_x H_\rho$ is approximately constant. In the following we refer to wavenumbers normalized by $1/H_\rho$ as κ, and since the horizontal wavelength is in the range $6-8\,H_\rho$, we have $\kappa \equiv k_x H_\rho \approx 1.0-0.8$. As H_ρ decreases, the vertical extent of the structures (in absolute units) shrinks by the same factor, so the effective k_z/k_x is approximately unity and thus $k \approx \sqrt{2}k_x$, so $\kappa \equiv k H_\rho \approx 1.5-1.1$. This shows that the growth rate for an isothermal atmosphere is fully determined by the coefficient $k_{\mathrm{f}}H_\rho$. If it is too small with respect to the strength of turbulent diffusion, the instability will not work.

In stellar mixing-length theory one assumes that the typical scale of the turbulent eddies is the mixing length $[\ell_{\mathrm{mix}}]$, given by

$$\ell_{\mathrm{mix}} \approx \alpha_{\mathrm{mix}} H_p, \tag{25}$$

where $\alpha_{\mathrm{mix}} \approx 1.6$ is an empirical dimensionless mixing-length parameter and $H_p \approx \gamma H_\rho$ is the pressure scale height with $\gamma \approx 5/3$ being the ratio of specific heats. Thus, using $k_{\mathrm{f}} =$
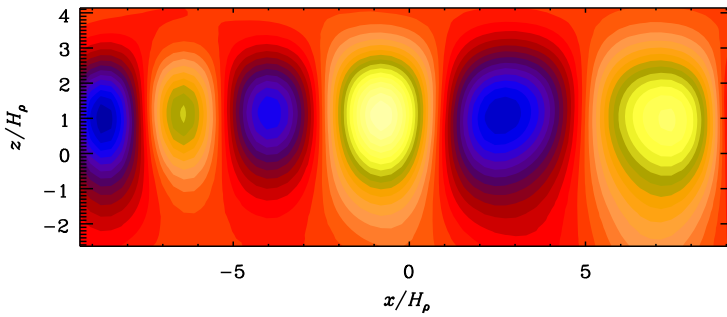
Figure 10 $\overline{B}_y$ in a setup similar to the first simulation from Figure 7 but with gravity three times stronger (or scale height three times smaller), taken at an early time.

$2\pi/\ell_{\mathrm{mix}}$, we have $\kappa_{\mathrm{f}} \equiv k_{\mathrm{f}} H_\rho \approx 2.4$. In that case the growth rate given in Equation (13) becomes

$$\frac{\lambda}{\eta_{\mathrm{t}} k^2} \approx 3\beta_\star \frac{k_{\mathrm{f}} H_\rho}{(k H_\rho)^2} - 1 = 3\beta_\star \frac{\kappa_{\mathrm{f}}}{\kappa^2} - 1. \qquad (26)$$

Using $\beta_\star \approx 0.23$ (Kemel *et al.*, 2012a), $\kappa_{\mathrm{f}} = 2.4$, and $\kappa = 1.5 - 1.1$, we find $\lambda/\eta_{\mathrm{t}} k^2 = -0.3 \ldots + 0.4$. On the other hand, using the convection-zone model of Spruit (1974) uses a larger value of α_{mix} such that $\kappa_{\mathrm{f}} \approx 3.3$ and thus $\lambda/\eta_{\mathrm{t}} k^2 = 0 \ldots + 0.9$, so the possibility of NEMPI under solar conditions hinges on details of the model. Next, for the near-surface shear layer at a depth of $20 - 40\,\mathrm{Mm}$ we estimate

$$\eta_{\mathrm{t}} k^2 \approx \frac{u_{\mathrm{rms}}}{3 k_{\mathrm{f}}} \frac{\kappa^2}{H_\rho^2} \approx \frac{u_{\mathrm{rms}}}{3 H_\rho} \frac{\kappa^2}{\kappa_{\mathrm{f}}} = 0.2 - 0.3 \frac{u_{\mathrm{rms}}}{H_\rho} = \frac{1}{2 - 5\,\mathrm{days}}, \qquad (27)$$

while for the Spruit model the *e*-folding time would be $1 - 3$ days. In this depth range the pressure scale height is $7 - 13\,\mathrm{Mm}$, so the density scale height is $12 - 22\,\mathrm{Mm}$, and thus the typical scale of flux concentrations is $80 - 150\,\mathrm{Mm}$. (We recall that in our isothermal model NEMPI can occur at any depth, just depending on the field strength.)

In the Sun, many other effects play a role, for example the convective turbulence is strongly anisotropic with vertical motions dominating over horizontal ones, thus causing negative radial shear in the surface layers (Kitchatinov and Rüdiger, 2005). This may cause new effects that could either enhance or diminish the vertical coupling of different layers. Whether the final outcome still leads to structures resembling active regions can only be answered by performing calculations in which such vertical variations of the stratification are taken into account.

6. Conclusions

The present work has demonstrated that NEMPI is able to concentrate the magnetic field into large patches encompassing the size of many turbulent eddies. The physics of this instability is principally different from the usual interchange instability of continuous magnetic fields (Parker, 1966, 1979; Hughes and Proctor, 1988; Cattaneo and Hughes, 1988; Wissink *et al.*, 2000; Isobe *et al.*, 2005; Kersalé, Hughes, and Tobias, 2007), because here the energy source of the instability is turbulent energy as opposed to gravitational energy.

Furthermore, we are here concerned with a turbulent medium, and so the sign of the buoyancy force is reversed in a regime of intermediate field strength. We have here re-examined the simple case of an isothermal layer in which NEMPI can in principle occur at any depth whose value is determined by the strength of the imposed field. Our new DNS have verified that the growth rate is indeed independent of the strength of the imposed field, provided that the peak of the instability fits still comfortably within the domain. During the subsequent nonlinear evolution of the instability, the overall density stratification readjusts, allowing the magnetic-field concentrations to move further down. It is important to realize that the resulting structures are subject to significant turbulent entrainment (Rieutord and Zahn, 1995), so their boundaries are not closed. The agreement with corresponding mean-field models is remarkable and much more convincing than what has been possible to demonstrate in mean-field dynamo theory. Mean-field models provide therefore a strong source of guidance when designing new setups for DNS.

While NEMPI now begins to be fairly well understood for isothermal models, more work is required for non-isothermal ones. In that case, the density scale height is no longer constant and the degree of stratification is much stronger at the top than in deeper layers. The simple result that the instability can occur at any height, depending just on the strength of the imposed field, is then no longer so obvious. At the same time, there is another, perhaps more important, aspect: the possibility of other instabilities. One of them is connected with the suppression of turbulent convective-energy flux by the mean magnetic field. As shown by Kitchatinov and Mazur (2000), this effect can also lead to magnetic-flux concentrations and it may be sustained for much stronger magnetic-field strengths, thus allowing the formation of structures in which the magnetic pressure becomes comparable to the ambient gas pressure. There may also be a connection with flux-segregation events seen in simulations of magneto-convection at large aspect ratios (Tao *et al.*, 1998; Kitiashvili *et al.*, 2010), which have already been shown to produce bipolar regions in simulations with radiation transfer (Stein *et al.*, 2011). The study of the possibility of producing sunspots similar to those of Rempel (2011a, 2011b), but without initial flux structures, is now of high priority in the quest for solving the solar dynamo problem in terms of distributed dynamo models in which magnetic activity is explained as a surface phenomenon.

Appendix A: Growth rate of NEMPI

In this appendix we derive the growth rate of NEMPI, neglecting for simplicity dissipation processes, using the anelastic approximation, and assuming $H_\rho = $ constant and $\nabla_y = 0$. However, in contrast to the simplistic derivation of Equation (8), we employ here a consistent treatment of lateral pressure variations in the equation of motion, ignoring in Equation (20) the $\overline{U} \cdot \nabla \overline{U}$ nonlinearity,

$$\frac{\partial \overline{U}(t, x, z)}{\partial t} = -\frac{1}{\rho} \nabla p_{\text{tot}} + \boldsymbol{g}, \qquad (28)$$

where $p_{\text{tot}} = \overline{p} + p_{\text{eff}}$ is the total pressure (the sum of the mean gas pressure [$\overline{p}$] and the effective magnetic pressure [p_{eff}]). We shall take into account that the mean magnetic field

is independent of y, so the mean magnetic tension vanishes. Taking twice the curl of Equation (28), and noting that $\hat{z} \cdot \nabla \times \nabla \times \overline{U} = -\Delta \overline{U}_z + \nabla_z \nabla \cdot \overline{U}$, we obtain

$$\frac{\partial}{\partial t}\left[\Delta \overline{U}_z + \nabla_z(\overline{U} \cdot \nabla \ln \overline{\rho})\right] = \hat{z} \cdot \nabla \times \nabla \times \left(\frac{p_{\text{tot}}}{\overline{\rho}^2}\nabla \overline{\rho}\right), \tag{29}$$

where we have used the anelastic approximation in the form $\nabla \cdot \overline{U} = -\overline{U} \cdot \nabla \ln \overline{\rho}$ [see the derivation of Equation (4)] and the fact that under the curl the gradient can be moved to $\overline{\rho}$. If we were to ignore variations of the density, the right-hand side would reduce to $\nabla_x^2 p_{\text{eff}}/\overline{\rho} H_\rho$. In the following, however, we retain such variations, which result from the fact that $q_p = q_p(\beta)$ depends both on $\overline{B}$ and on $\overline{\rho}$. The right-hand side of Equation (29) can be simplified to give

$$\hat{z} \cdot \nabla \times \nabla \times \left(\frac{p_{\text{tot}}}{\overline{\rho}^2}\nabla \overline{\rho}\right) = \nabla_x\left[\left(\nabla_z \frac{p_{\text{tot}}}{\overline{\rho}}\right)\frac{\nabla_x \overline{\rho}}{\overline{\rho}} - \left(\nabla_x \frac{p_{\text{tot}}}{\overline{\rho}}\right)\frac{\nabla_z \overline{\rho}}{\overline{\rho}}\right]. \tag{30}$$

We linearize, indicating small changes by δ or subscript 1, as in Section 1, and note that

$$\delta\left(\frac{p_{\text{tot}}}{\overline{\rho}}\right) = \frac{1}{2}v_A^2\left(1 - q_p - dq_p/d\ln\beta^2\right)\left(2\frac{\delta \overline{B}_y}{B_0} - \frac{\delta \overline{\rho}}{\overline{\rho}}\right), \tag{31}$$

while

$$\nabla_z\left(\frac{p_{\text{tot}}}{\overline{\rho}}\right) = \frac{1}{2}v_A^2\left(1 - q_p - dq_p/d\ln\beta^2\right)\frac{1}{H_\rho}. \tag{32}$$

Inserting this into Equation (30), the $\delta\rho$ term in Equation (31) cancels the linearized form of $\nabla_x \overline{\rho}$ in Equation (30), and we are left with

$$\frac{\partial}{\partial t}\left(\Delta - \frac{1}{H_\rho}\nabla_z\right)\delta \overline{U}_z = 2\frac{v_A^2}{H_\rho}\frac{d\mathcal{P}_{\text{eff}}}{d\beta^2}\frac{\nabla_x^2 \delta \overline{B}_y}{B_0}, \tag{33}$$

where we have used Equation (14). Introducing a new variable $V_z = \sqrt{\overline{\rho}}\,\delta\overline{U}_z$, and rewriting Equation (33) for V_z, we obtain

$$\frac{\partial}{\partial t}\left(\Delta - \frac{1}{4H_\rho^2}\right)V_z = 2\sqrt{\overline{\rho}}\,\frac{v_A^2}{H_\rho}\frac{d\mathcal{P}_{\text{eff}}}{d\beta^2}\frac{\nabla_x^2 \delta \overline{B}_y}{B_0}. \tag{34}$$

Using the linearized form of Equation (6), we arrive at the following equation:

$$\frac{\partial^2}{\partial t^2}\left(\Delta - \frac{1}{4H_\rho^2}\right)V_z(t,x,z) = -\frac{2v_A^2}{H_\rho^2}\frac{d\mathcal{P}_{\text{eff}}}{d\beta^2}\nabla_x^2 V_z. \tag{35}$$

It follows from Equation (35) that a necessary condition for the large-scale instability is

$$\frac{d\mathcal{P}_{\text{eff}}}{d\beta^2} < 0. \tag{36}$$

For instance, in the WKB approximation when $k_z H_\rho \gg 1$, $i.e.$ when the characteristic scale of the spatial variation of the perturbations of the magnetic and velocity fields are much smaller than the density height length [H_ρ], the growth rate of the instability reads

$$\lambda = \frac{v_A}{H_\rho}\left(-2\frac{d\mathcal{P}_{\text{eff}}}{d\beta^2}\right)^{1/2}\frac{k_x}{k}. \tag{37}$$

For an arbitrary vertical inhomogeneity of the density, we seek a solution of Equation (35) in the form $V_z(t,x,z) = V(z)\exp(\lambda t + ik_x x)$ and obtain an eigenvalue problem:

$$\lambda_0^{-2}(z)\left[1 + k_x^{-2}\left(\frac{1}{4H_\rho^2} - \nabla_z^2\right)\right]V_z = \lambda^{-2}V_z, \tag{38}$$
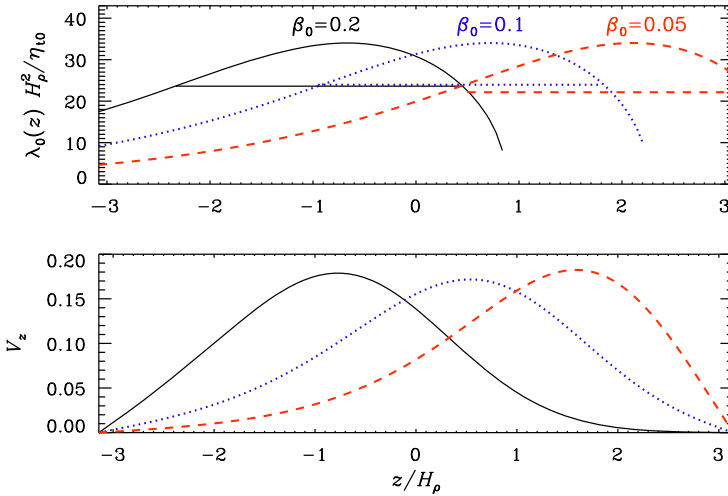
Figure 11 Upper panel: comparison between the graphs of $\lambda_0(z)$ and the corresponding eigenvalues $[\lambda]$ (horizontal lines segments) for $B_0/B_{\mathrm{eq}0} = 0.05$, 0.1, and 0.2. Lower panel: eigenfunctions $[V_z(z)]$ for the same three cases obtained by solving Equation (38).

where λ^{-2} is the eigenvalue and

$$\lambda_0(z) = \frac{v_{\mathrm{A}}(z)}{H_\rho} \left(-2\frac{\mathrm{d}\mathcal{P}_{\mathrm{eff}}(z)}{\mathrm{d}\beta^2} \right)^{1/2}. \tag{39}$$

We are interested in the fastest growing solutions, corresponding to the maximum value of λ. We find the maximum value of λ by discretizing Equation (38) on a grid, using a second-order finite-difference scheme for the derivatives, and solving the resultant eigenvalue problem numerically. In Figure 11 the resulting values of λ are compared with $\lambda_0(z)$ and the profiles of $V_z(z)$. The values of λ turn out to be about twice as large as the actual growth rates found in the fully compressible mean-field models, where viscosity and magnetic diffusion are included. A reasonable improvement would be to subtract the damping rate $[\eta_t k^2]$ from the ideal growth rates $[\lambda]$; see Equation (9). In Figure 12 we compare $\lambda(k_x)$ with attenuated growth rates $[\lambda(k_x) - \eta_t k^2]$ for different values of η_t, assuming that the effective wavenumber obeys $k^2 \approx 2k_x^2$, as explained in paragraph (iii) of Section 5.

It is customary to obtain approximate analytic solutions to Equation (38) as marginally bound states of an associated Schrödinger equation, $\Psi'' - \tilde{U}(R)\,\Psi = 0$, via the transformation

$$\Psi(R) = \sqrt{R}\, V(z), \qquad R(z) = \frac{v_{\mathrm{A}0}^2}{u_{\mathrm{rms}}^2 \beta_{\mathrm{p}}^2}\, e^{z/H_\rho}, \tag{40}$$

where $\overline{\rho} = \overline{\rho}_0\, e^{-z/H_\rho}$ is used as mean density profile, $v_{\mathrm{A}0} = B_0/\sqrt{\overline{\rho}_0}$ is the Alfvén speed based on the averaged density, and

$$\tilde{U}(R) = \frac{k_x^2}{R} \left[\frac{H_\rho^2}{R} + a\left(1 - \frac{q_{\mathrm{p}0}}{(1+R)^2} \right) \right] \tag{41}$$

is the potential with

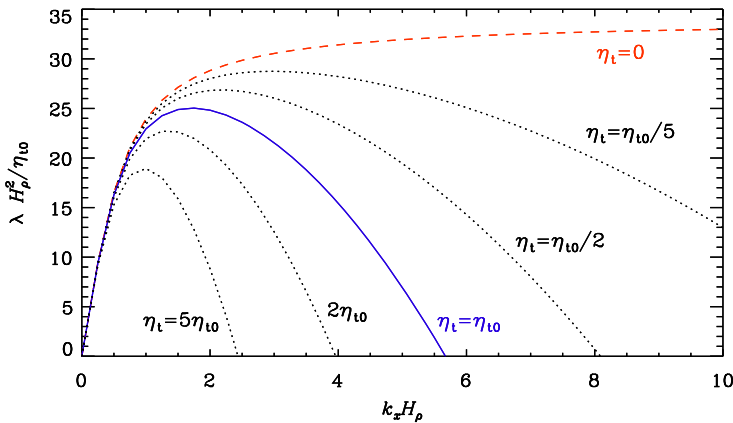$$a = \frac{u_{\mathrm{rms}}^2 \beta_{\mathrm{p}}^2}{\lambda^2} \tag{42}$$

Figure 12 Growth rates obtained by solving Equation (38) for $B_0/B_{eq0} = 0.1$ as a function of k_x for the case $\eta_t = 0$ (dashed lines) compared with cases with different values of η_t (dotted lines). The solid line applies to the case $\eta_t = \eta_{t0}$.
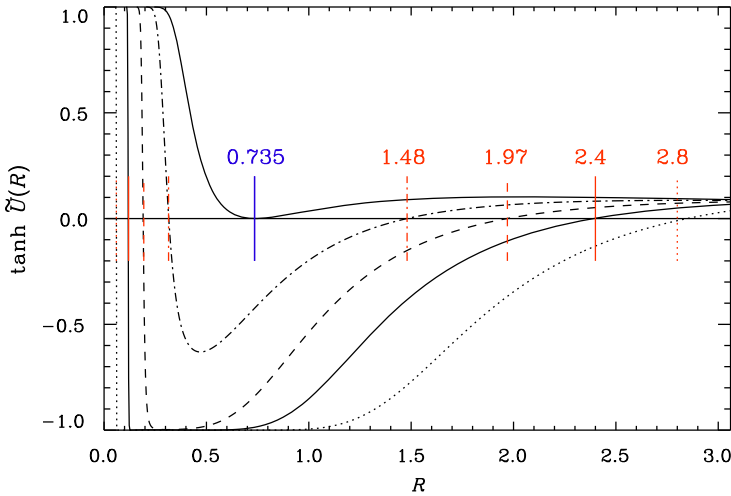

Figure 13 $\tanh \tilde{U}(R)$ for $a = 0.24$ (dash–triple–dotted line, $\tilde{\lambda} = 0.034$, $R_1 = R_2 = 0.735$), $a = 0.3$ [dash–dotted line, $\tilde{\lambda} = 0.030$, $(R_1, R_2) = (0.32, 1.5)$], $a = 0.4$ [dashed line, $\tilde{\lambda} = 0.026$, $(R_1, R_2) = (0.19, 1.9)$], $a = 0.56$ [solid line, $\tilde{\lambda} = 0.022$, $(R_1, R_2) = (0.12, 2.4)$], and $a = 1$ [dotted line, $\tilde{\lambda} = 0.017$, $(R_1, R_2) = (0.06, 2.8)$].

being a new eigenvalue. The potential [$\tilde{U}(R)$] has the following asymptotic behavior: $\tilde{U}(R \to 0) = k_\perp^2 H_\rho^2/R^2$ and $\tilde{U}(R \to \infty) = a/R$. For the existence of the instability, the potential $\tilde{U}(R)$ should have a negative minimum. For example, for a long wavelength instability ($k_\perp^2 H_\rho^2 \ll 1$) and when $q_{p0} > 1$, the potential $\tilde{U}(R)$ has a negative minimum, and the instability can be excited.

When the potential $\tilde{U}(R)$ has a negative minimum and since $\tilde{U}(R \to 0) > 0$ and $\tilde{U}(R \to \infty) > 0$, there are two points R_1 and R_2 (the so-called turning points) at which $\tilde{U}(R) = 0$. We have computed $\tilde{U}(R)$ for several values of a/H_ρ; see Figure 13, were we plot $\tanh \tilde{U}(R)$ to show more clearly the position of the turning points. Here we quote the nondimensional

values of $\tilde{\lambda} \equiv \lambda H_\rho / c_s$. It turns out for $a \approx 0.241\, H_\rho$ the turning points collapse to $R_1 = R_2 \approx 0.735$. The numerically computed maximum value of λ corresponds to $a \approx 0.56\, H_\rho$, where the turning points are $R_1 \approx 0.735$ and $R_2 \approx 2.4$. Using the equations $\tilde{U}(R_{1,2}) = 0$ together with Equations (41) and (42), we obtain the growth rate of the instability as

$$\lambda = \frac{\beta_\star u_{\mathrm{rms}}}{H_\rho} \frac{[R_1 R_2(2 + R_1 + R_2)]^{1/2}}{(1 + R_1)(1 + R_2)}, \tag{43}$$

where we have used $\beta_\star = \beta_p \sqrt{q_{p0}}$. Note that Equation (43) is consistent with the simple estimate (12). In the critical case where $R = R_1 = R_2$, we find an upper bound of $\lambda \leq \sqrt{2}\beta_\star u_{\mathrm{rms}} R / H_\rho (1 + R)^{3/2}$.

References

Arlt, R., Sule, A., Rüdiger, G.: 2007, *Astron. Astrophys.* **461**, 295.

Bai, T.: 1987, *Astrophys. J.* **314**, 795.

Bai, T.: 1988, *Astrophys. J.* **328**, 860.

Benevolenskaya, E.E., Hoeksema, J.T., Kosovichev, A.G., Scherrer, P.H.: 1999, *Astrophys. J. Lett.* **517**, L163.

Bigazzi, A., Ruzmaikin, A.: 2004, *Astrophys. J.* **604**, 944.

Bogart, R.S.: 1982, *Solar Phys.* **76**, 155. doi:10.1007/BF00214137.

Brandenburg, A.: 2005, *Astrophys. J.* **625**, 539. doi:10.1086/429584.

Brandenburg, A., Kemel, K., Kleeorin, N., Mitra, D., Rogachevskii, I.: 2011, *Astrophys. J. Lett.* **740**, L50. doi:10.1088/2041-8205/740/2/L50.

Brandenburg, A., Kemel, K., Kleeorin, N., Rogachevskii, I.: 2012, *Astrophys. J.* **749**, 179. doi:10.1088/0004-637X/749/2/179.

Brandenburg, A., Kleeorin, N., Rogachevskii, I.: 2010, *Astron. Nachr.* **331**, 5. doi:10.1002/asna.201111638.

Cally, P.S., Dikpati, M., Gilman, P.A.: 2003, *Astrophys. J.* **582**, 1190.

Cattaneo, F., Hughes, D.W.: 1988, *J. Fluid Mech.* **196**, 323.

Charbonneau, P.: 2010, *Living Rev. Solar Phys.* **7**, 3. http://www.livingreviews.org/lrsp-2010-3.

Choudhuri, A.R., Gilman, P.A.: 1987, *Astrophys. J.* **316**, 788.

D'Silva, S., Choudhuri, A.R.: 1993, *Astron. Astrophys.* **272**, 621.

Epstein, T.: 1904, *Astron. Nachr.* **166**, 333.

Fan, Y.: 2009, *Living Rev. Solar Phys.* **6**, 4. http://www.livingreviews.org/lrsp-2009-4.

Golub, L., Vaiana, G.S.: 1980, *Astrophys. J. Lett.* **235**, L119.

Golub, L., Rosner, R., Vaiana, G.S., Weiss, N.O.: 1981, *Astrophys. J.* **243**, 309.

Hindman, B.W., Haber, D.A., Toomre, J.: 2009, *Astrophys. J.* **698**, 1749.

Hughes, D.W., Proctor, M.R.E.: 1988, *Ann. Rev. Fluid Dyn.* **20**, 187.

Ilonidis, S., Zhao, J., Kosovichev, A.: 2011, *Science* **333**, 993.

Isobe, H., Miyagoshi, T., Shibata, K., Yokoyama, T.: 2005, *Nature* **434**, 478.

Käpylä, P.J., Brandenburg, A., Kleeorin, N., Mantere, M.J., Rogachevskii, I.: 2012, *Mon. Not. Roy. Astron. Soc.* doi:10.1111/j.1365-2966.2012.20801.x, arXiv:1105.5785.

Kemel, K., Brandenburg, A., Kleeorin, N., Mitra, D., Rogachevskii, I.: 2012a, *Solar Phys.* doi:10.1007/s11207-012-9949-0, arXiv:1112.0279.

Kemel, K., Brandenburg, A., Kleeorin, N., Rogachevskii, I.: 2012b, *Astron. Nachr.* **333**, 95. doi:10.1002/asna.201111638.

Kersalé, E., Hughes, D.W., Tobias, S.M.: 2007, *Astrophys. J. Lett.* **663**, L113.

Kitchatinov, L.L., Mazur, M.V.: 2000, *Solar Phys.* **191**, 325. doi:10.1023/A:1005213708194.

Kitchatinov, L.L., Rüdiger, G.: 2005, *Astron. Nachr.* **326**, 379.

Kitiashvili, I.N., Kosovichev, A.G., Wray, A.A., Mansour, N.N.: 2010, *Astrophys. J.* **719**, 307.

Kleeorin, N., Mond, M., Rogachevskii, I.: 1996, *Astron. Astrophys.* **307**, 293.

Kleeorin, N., Rogachevskii, I.: 1994, *Phys. Rev. E* **50**, 2716.

Kleeorin, N.I., Rogachevskii, I.V., Ruzmaikin, A.A.: 1989, *Sov. Astron. Lett.* **15**, 274.

Kleeorin, N.I., Rogachevskii, I.V., Ruzmaikin, A.A.: 1990, *Sov. Phys. JETP* **70**, 878.

Kosovichev, A.G.: 2002, *Astron. Nachr.* **323**, 186.

Kosovichev, A.G., Stenflo, J.O.: 2008, *Astrophys. J. Lett.* **688**, L115.

Parker, E.N.: 1966, *Astrophys. J.* **145**, 811.

Parker, E.N.: 1979, *Cosmical Magnetic Fields*, Oxford University Press, New York.

Pipin, V.V., Kosovichev, A.G.: 2011, *Astrophys. J. Lett.* **727**, L45.

Rempel, M.: 2011a, *Astrophys. J.* **729**, 5.

Rempel, M.: 2011b, *Astrophys. J.* **740**, 15.

Rieutord, M., Zahn, J.-P.: 1995, *Astron. Astrophys.* **296**, 127.

Rogachevskii, I., Kleeorin, N.: 2007, *Phys. Rev. E* **76**, 056307.

Ruzmaikin, A.: 1998, *Solar Phys.* **181**, 1. doi:10.1023/A:1016563632058.

Sanford, F.: 1941, *Science* **94**, 18.

Schatten, K.H.: 2007, *Astrophys. J. Suppl.* **169**, 137.

Schüssler, M., Caligari, P., Ferriz-Mas, A., Moreno-Insertis, F.: 1994, *Astron. Astrophys. Lett.* **281**, L69.

Spruit, H.C.: 1974, *Solar Phys.* **34**, 277. doi:10.1007/BF00153665.

Stein, R.F., Lagerfjärd, A., Nordlund, Å., Georgobiani, D.: 2011, *Solar Phys.* **268**, 271.

Stein, R.F., Leibacher, J.: 1974, *Ann. Rev. Astron. Astrophys.* **12**, 407.

Stenflo, J.O., Kosovichev, A.G.: 2012, *Astrophys. J.* **745**, 129.

Tao, L., Weiss, N.O., Brownjohn, D.P., Proctor, M.R.E.: 1998, *Astrophys. J. Lett.* **496**, L39.

Tayler, R.J.: 1973, *Mon. Not. Roy. Astron. Soc.* **161**, 365.

Vitinskij, J.I.: 1969, *Solar Phys.* **7**, 210. doi:10.1007/BF00224899.

Wissink, J.G., Hughes, D.W., Matthews, P.C., Proctor, M.R.E.: 2000, *Mon. Not. Roy. Astron. Soc.* **318**, 501.

Zhao, J., Kosovichev, A.G., Duvall, T.L. Jr.: 2001, *Astrophys. J.* **557**, 384.